An experimental and numerical study for the damage characterization of a Ti–6AL–4V titanium alloy

Nima Allahverdizadeh, Andrea Gilioli, Andrea Manes *, Marco Giglio

Politecnico di Milano, Dipartimento di Meccanica, Via la Masa 1, Milano 20156, Italy

1. Introduction

The study of material damage in structures plays an important role in the design process. Comprehension of the damage behavior of the materials can be used to define and properly calibrate the criteria, which can be adopted for numerical simulations reducing the risks and cost of possible catastrophic failures. Focusing on ductile metals several damage models have been proposed in the last decades, which are based on different physical approaches. However, all of these models can be classified into three main groups:

- phenomenological models,
- porosity models,
- continuum damage mechanics (CDM) models.

Johnson–Cook [1],Rice–Tracey [2], Leroy et al. [3], Cockroft–Latham [4] are some of the most famous phenomenological damage models. Phenomenological models are increasingly used for many industrial applications due to their relatively easy calibration procedure and their wide implementation in several commercial finite element codes. According to these models, failure occurs abruptly when a damage parameter reaches a critical value. Generally, phenomenological models are uncoupled, hence their base assumption is that the damage process does not affect the plastic behavior of the material. This assumption makes phenomenological models relatively easy to implement and to calibrate; however, the main drawback of these models is that they are aimed at estimating the failure without considering the relevant physical background. In the last decade, several new phenomenological models have been proposed aimed at reproducing the ductile failure phenomenon more closely. The Bao–Wierzbicki model [5,6] and the modified Mohr–Coulomb model [7,8] are two widely used phenomenological models due to promising results in their applications of failure simulations of different and extreme load conditions on real components [54] and due to their quite good geometry transfer-ability [9–11]. It is well known that stress triaxiality plays an important role in the ductile fracture [12–14]. However, recently also the importance of another parameter, called the Lode angle, has been highlighted in several publications including Bai and Wierzbicki [7,8]. The Modified Mohr–Coulomb damage criterion considers also this effect on fracture. Therefore, the fracture locus is no longer simply a curve in a 2D plane (stress triaxiality–failure strain) but it is rather a surface in a 3D space (triaxiality–Lode angle–failure strain).

Porosity models are another approach to investigate fracture. These models are based on micromechanical concepts and are much more complex to calibrate, compared with phenomenological ones. Damage and plasticity are also coupled in these models

* Corresponding author.
E-mail addresses: nima.allahverdizadeh@polimi.it (N. Allahverdizadeh), andrea.gilioli@polimi.it (A. Gilioli), andrea.manes@polimi.it (A. Manes), marco.giglio@polimi.it (M. Giglio).

Notations

A_{ef}^n	CDM, effective resisting area of the intersection plane, which is reduced due to damage
A_0^n	CDM, nominal intersection area of the plane and the reference volume before damage
BW	Bao–Wierzbicki damage criterion
CDM	continuum damage mechanics
D	CDM, isotropic damage variable
D_{cr}	critical value of damage
D_n	CDM, damage variable in the direction of the normal vector n
F_D	damage dissipation potential
G	shear modulus
JC	Johnson–Cook damage criterion
K	bulk modulus
MMC	modified Mohr–Coulomb criterion
q	second stress invariant
R	isotropic hardening internal variable
r	third stress invariant
S	parameter related to the evolution of damage
T	temperature
Y	damage energy release rate

Greek notations

γ	plastic multiplier
ε	strain tensor
ε^e	elastic strain tensor
ε^p	plastic strain tensor
$\bar{\varepsilon}$	equivalent strain
ε_f	failure strain
ε_p	equivalent plastic strain, PEEQ
ε_{th}	threshold strain
η	stress triaxiality
η_{av}	average stress triaxiality
$\bar{\theta}$	Lode angle parameter
$\bar{\theta}_{av}$	average Lode angle parameter
ξ	normalized third stress invariant
σ	stress tensor
σ_{eff}	effective stress
σ_h	hydrostatic stress
σ_n	normal stress
σ_{vm}	von Mises equivalent stress
σ_{y0}	initial yield stress
τ	shear stress
ϕ	yield function

and the damage therefore affects the plasticity behavior of the material. The Gurson–Tvergaard–Needleman [15,16] model is the most important porosity model and nine parameters have to be determined for its calibration.

A further framework for damage investigations is the continuum damage mechanics (CDM). CDM models differ significantly from phenomenological models because plasticity and damage are coupled. Damage is described by a continuous parameter which evolves during the loading and reaches its maximum value at the onset of failure, however its effect on the material behavior is already present even before failure. Lemaitre [17] proposed the first CDM model based on the pioneer articles of Chaboche [18] and Kachanov [19], aiming to describe ductile damage. In the last decades various CDM models have been proposed [20–23] and the application of the CDM models has been extended to cover more complex material behavior [24–32].

It is common practice to calibrate a model for a specific configuration (load, geometry,…) and afterwards extend the calibration to other scenarios, see [54]. The drawback of such an extrapolative approach is that it can, in some circumstances, lead to relevant errors. In order to minimize errors, damage models should therefore be investigated for a wide range of loading conditions which would could lead to unfeasible costs. In the last few years, some studies investigated the applicability of different damage models for different loading conditions. Choung [33] has studied API-2W50 and DNV-DH32TM steel, adopting smooth, notched round and flat specimens and comparing the shear fracture model, Lemaitre's CDM model and Gurson's one. Coppola et al. [34] has compared three different steel grades carrying out tensile, torsion and bending tests, covering a wide range of stress triaxiality and Lode angles and focusing on the investigation of the effect of the Lode angle on the fracture locus. Wierzbicki et al. [35] and Bao and Wierzbicki [36] have studied 2024-T351 aluminum alloy performing upsetting and tensile tests on various specimen geometries, investigating different phenomenological models and subsequently comparing the results with the experimental data. Geometry transferability of the Bonora's CDM model parameters in ferritic steels has been investigated by Bonora et al. [37] both for low and high triaxiality. One of the most comprehensive studies of the application of different ductile damage criteria in very different scenarios is by Li et al. [38] on an Al6061-T6 aluminum alloy. The authors performed tensile and compression tests on different geometries including flat and round specimens and they studied the failure predictions of several damage models, including phenomenological models, the Gurson–Tvergaard–Needleman (GTN) porosity model and Lemaitre's CDM model.

In spite of the abovementioned studies, more research is still needed to investigate the geometry transferability of the damage models. Therefore, in this paper the modified Mohr–Coulomb, one of the most recent and complete phenomenological damage models, and Lemaitre's model, as the most important and most used CDM, have been investigated. The critical aspects of each model have been highlighted with particular attention and the advantages and disadvantages of each approach, have been pointed out. A large experimental test program has been carried out on various specimen geometries and under different loading conditions in order to cover a wide range of stress triaxiality and Lode angles. Torsion plus tension/compression tests and tensile tests on smooth, notched round and flat specimens have been carried. Load–displacement/torque–rotation data have been obtained from experimental tests and the results have been used for calibration by means of FE models. Specifically the MMC model has been calibrated on the basis of all the experimentally collected data (excluding the TPBT data which have been adopted only for validation purpose, therefore 13 experimental points have been considered for the "base calibration") while only the tensile test of the round smooth specimen has been used for the calibration of the CDM model. Eventually, calibration parameters of both the MMC and CDM models have been obtained for a Ti–6Al–4V titanium alloy. This material has been chosen due to its high strength and low volumic mass, which make it a very commonly used material in the aerospace industry for critical components. Moreover, regardless of the importance of Ti–6Al–4V, only few studies have investigated its fracture [9,10,39].

2. Experiments

2.1. Ti–6Al–4V titanium alloy

Ti–6Al–4V is the most widely used titanium alloy, accounting for more than 50% of the total titanium usage. Ti–6Al–4V belongs to the category of the alpha+beta alloys, it can be strengthened by

heat treatment or by thermo mechanical processing and has useful creep resistance up to 300 °C, excellent fatigue strength, and a fair weldability. Regarding aerospace applications, it is adopted for aircraft gas turbine disks and blades and for helicopter main rotor hubs. Relevant industrial fields where Ti–6Al–4V alloy is used are aerospace, marine, offshore and power generation industries (ASME metals handbook, vol. 2 [40]). Table 1 shows the chemical composition of the Ti–6AL–4V titanium alloy. Fig. 1 shows the microstructure of the tested Ti–6Al–4V titanium alloy. This image has been taken from the etched surface of the material using an optical microscope. Kroll's reagent (94 ml distilled water, 5 ml nitric acid and 1 ml hydrofluoric acid) was used for surface etching. The alpha+beta phases are clearly visible in Fig. 1 and the average grain size is approximately 20 μm.

2.2. Experimental tests

In this research, an extensive test program has been designed and carried out to investigate the ductile fracture of a Ti–6Al–4V titanium alloy in a wide range of stress states and deformation modes. The development of an extensive experimental program along with a particular test system allowing simultaneous multi-axial loads (tension plus torsion) is one of the main characteristics of this research. The test program has been designed to cover a large range of loading conditions, characterized by different stress triaxiality and Lode angles. Load–displacement and torque–rotation data have been obtained from the experimental tests. They are the main data used for the evaluation of the accuracy and the reliability of the numerical results. Experiments include a range of triaxiality spacing from very low values, close to zero, until the medium-high triaxiality regions (slightly more than one). In order to evaluate such different stress states, different specimen geometries including notched and smooth round/flat specimens and several different load conditions, including uniaxial tensile, torsion and three-point bending, have been tested. Three different series of experiments have been performed. The first series includes uniaxial tensile tests on flat specimens (plane stress state): one

Table 1
Weight chemical composition of Ti–6Al–4V [41].

| Composition [wt%]							
Ti	**O**	**N**	**C**	**H**	**Al**	**Fe**	**V**
Bal.	0.16	0.01	0.01	0.001	6.38	0.15	4.17

shear dominant specimen and four specimens with medium triaxiality values. The second series of experiments has been performed on round specimen and includes multiaxial torsion tests. This series of experiments covers shear dominant, mixed shear and tensile dominant regions. One notched specimen under uniaxial tension has been also tested in the second series of tests whose triaxiality belongs to the medium-high region. The third and last series of experimental tests regards the three point bending test of a notched specimen, which is a relevant application to validate the transferability of the material models for different loading conditions. The three points bending test (TPBT) of a notched component is a particularly interesting test because it is an application characterized by a high stress/strain gradient while offering the advantage that it can be performed using a standard test system device, thus in a laboratory environment with reduced uncertainties. Basically the results from this test have been used for validation purpose (with some exception discussed herein). However the capability of the calibrated models has been assessed also by the replication (by means of numerical model) of all the tests in order to check the consistency of the models (formulation and calibrated parameters) in different loading conditions. The experimental program is explained in more detail in the following sections. A summary of all the experimental tests carried out in this research can be found in Table 2.

2.3. Flat specimens (plane stress)

The first test series is based on uniaxial monotonic tests on flat specimens designed to guarantee a plane stress condition. Different geometries with different notch radiuses have been designed and manufactured to cover a range of stress states including triaxiality values near zero and up to 0.6, and Lode angle between 0 and 1, see Fig. 2. The thickness of all specimens is 2 mm. Tests have been performed in displacement control using a MTS alliance RT/100 kN testing machine. An extensometer with an initial base length of 12.5 mm for the notched specimens and a 50 mm for the shear specimen has been used to measure the displacement during the tests. Fig. 3 shows flat specimens after failure.

2.4. Uni and multiaxial tests on round specimens

The second test series is based mainly on multi-axial tests (torsion+tension) performed on round specimens. The original experimental data and more information about the test set up and the experimental procedure can be found in [10]. Two different
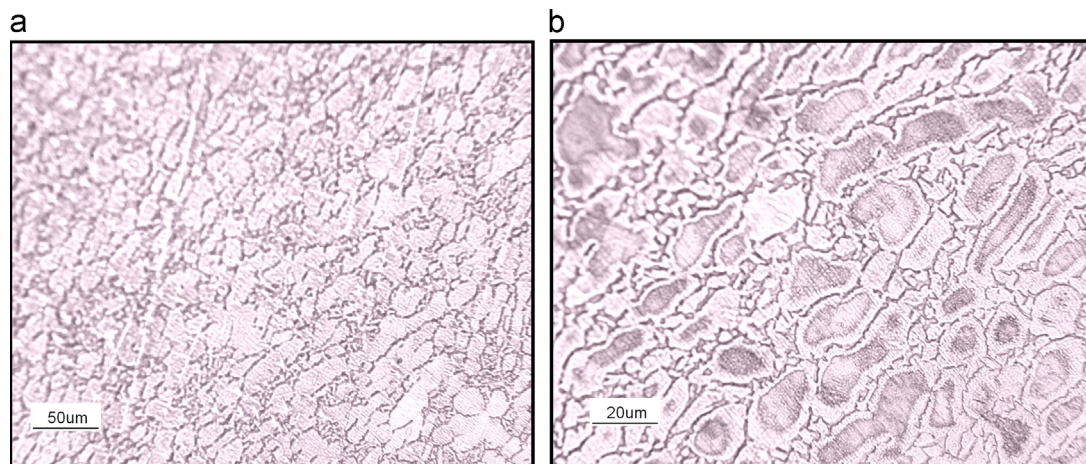
Fig. 1. Microstructure of the tested Ti–6Al–4V titanium alloy (a) 200 ×. (b) 500 ×.

Table 2
Summary of all experiments.

| Experimental series	Specimen type	Superimposed axial load (kN)	Experimental data
Flat specimens uniaxial tensile	Notch20 mm (no. 1)	–	Load–displacement data-extensometer 25 mm
	Notch10 mm (no. 2)	–	Load–displacement data-extensometer 25 mm
	Notch6.6 mm (no. 3)	–	Load–displacement data-extensometer 25 mm
	Hole (no. 4)	–	Load–displacement data-extensometer 25 mm
	Shear (no.5)	–	Load–displacement data-extensometer 50 mm
Tensile test	B (no. 7)	–	Load–displacement-extensometer 10 mm
	Smooth (no. 9)	–	Load–displacement-extensometer 12.5 mm
Torsion+tension/compression [10]	A (no. 6)	−24	Torque–rotation
	A (no. 6)	−10	Torque–rotation
	A (no. 6)	0	Torque–rotation
	A (no. 6)	20	Torque–rotation
	A (no. 6)	30	Torque–rotation
	A (no. 6)	40	Torque–rotation
Three point bending	Notched (no. 8)	–	Load–displacement (displacement of pusher) data
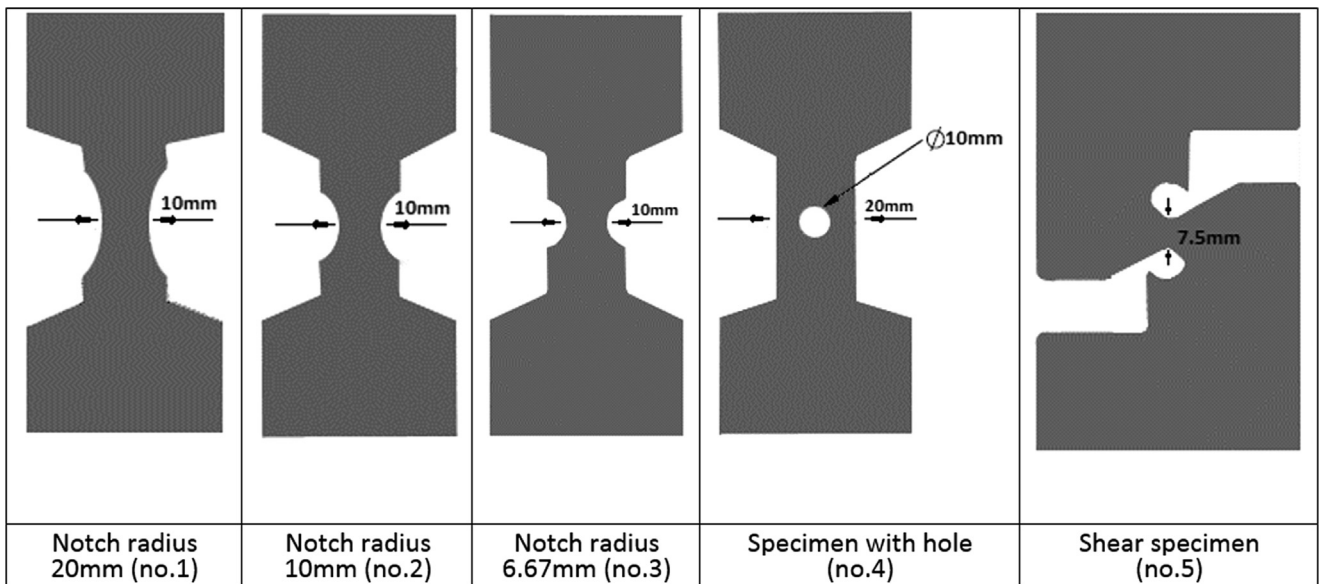
Fig. 2. Flat specimens' geometry.
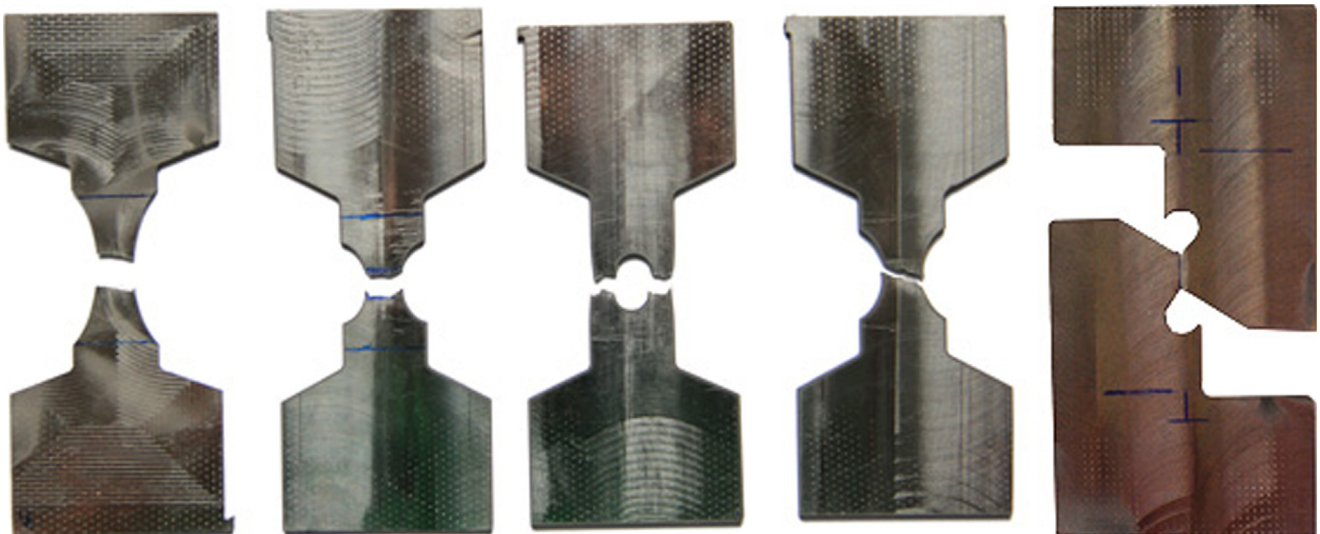
Fig. 3. Flat specimens after failure.

types of specimen geometries have been tested, see Fig. 4 for details. Specimen type A has been used for the pure torsion and for the multiaxial tension+torsion test while type B has been used for uniaxial tensile tests. The multi-axial test consists of the application of a pre-tensile constant load followed by a rotation ramp. The test has been performed in rotation control adopting a hydraulic MTS809 testing machine. Torque–rotation curves are the main output of the experiments.

Also a uniaxial tensile test on the notched specimen B has been carried out. An extensometer with the initial base length of 12.5 mm has been used to measure the displacement. A MTS alliance RT/150 kN testing machine has been used to perform the tension test.

2.5. Three point bending test

In order to perform a test in the medium high triaxiality region, a three point bending test on a sharp notched specimen has been performed. Fig. 5 shows the geometry and failure surface of the tested specimen. The test has been carried out adopting a uniaxial hydraulic testing machine. A laser sensor (MEL Mikroelektronik GMBH, M5L/20, range 20 mm) has been used to measure the displacement of the pusher. Load has been acquired by means of a load cell [10].

3. Theoretical background

3.1. Modified Mohr–Coulomb fracture locus

The modified Mohr–Coulomb is a very effective phenomenological ductile damage criterion compared with other criteria such as the Johnson–Cook [1] or Bao–Wierzbicki [5], as it takes into account not only the triaxiality but also the Lode angle effect in the fracture locus definition. Various studies highlighted that the Lode angle plays a key role in the ductile fracture of metals [42–44].

The original MC (Mohr–Coulomb) criterion has been commonly applied in rock and soil mechanics [45,46] and only recently in Bai and Wierzbicki [7] the importance of triaxiality and Lode angle has been acknowledged also for the ductile fracture of metals. The MMC is an extension of the original MC criterion whose description and
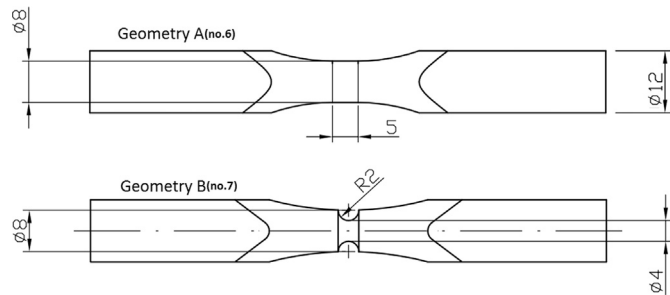

Fig. 4. Geometry of the specimens (nos. 6 and 7) in the second series of experiments (dimensions in mm).
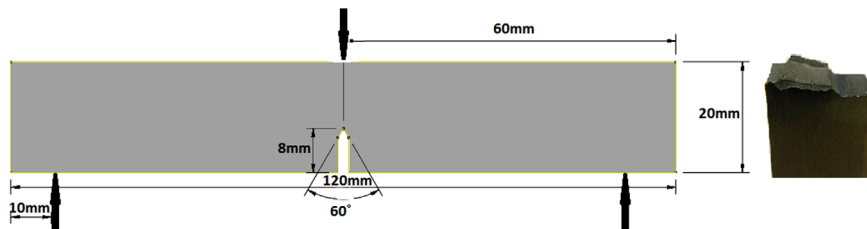
derivation can be found in [8]. The original MC criterion states that fracture happens when the combination of normal stress, σ_n and shear stress, τ reaches a critical value on a fracture plane, see Eq. (1)

$$(\tau + C_1 \sigma_n) = C_2 \tag{1}$$

C_1 and C_2 are material constants. In case $C_1 = 0$ the criterion is reduced to the maximal shear stress.

The Lode angle parameter can be defined as Eq. (2)

$$\overline{\vartheta} = 1 - \frac{2}{\pi} \arccos \xi \tag{2}$$

where ξ is the normalized third stress invariant which is calculated as Eq. (3)

$$\xi = \left(\frac{r}{\sigma_{vm}}\right)^3. \tag{3}$$

The Lode angle is strictly related to the third deviatoric stress invariant, and in particular, it describes the relationship between the intermediate principal stress and the minor and major principal stresses. The authors subsequently refer to the Lode angle parameter as the Lode angle for simplicity reasons even if it is not exactly the same quantity.

After the transformation of Eq. (1) into the space of stress invariants $\overline{\theta}$ and ξ, the final form of the MMC fracture locus is Eq. (4), [8]

$$\varepsilon_f = \left(\frac{A}{C_2} \left(C_3 + \frac{\sqrt{3}}{2-\sqrt{3}}(1-C_3)\left(\sec\left(\frac{\overline{\theta}\pi}{6}\right)-1\right)\right) \left(\sqrt{\frac{1+C_1^2}{3}} \cos\left(\frac{\overline{\theta}\pi}{6}\right) \right. \right.$$
$$\left. \left. + C_1 \left(\eta + \frac{1}{3} \sin\left(\frac{\overline{\theta}\pi}{6}\right) \right) \right) \right)^{-1/n} \tag{4}$$

Eq. (4) is valid for power type hardening materials. The criterion is based on five parameters but only three of them are related to fracture. Indeed A and n are derived from the plasticity law, hence only the parameters C_1, C_2, C_3 refer directly to fracture.

3.2. Lemaitre's model

Damage is considered as a thermodynamic state variable, which characterizes the deterioration of the material. The progressive damage of a ductile material is based on the change of the shape and the number of voids within the material. As a matter of fact, the load bearing capacity of the material decreases with the progression of the damage. Generally speaking, by considering a reference volume element at a given point, the damage variable can be defined by Eq. (5)

$$D_n = 1 - \frac{A_{ef}^n}{A_0^n} \tag{5}$$

where A_{ef}^n is the effective resisting area of the intersection plane, A_0^n is the nominal intersection area of the plane and the reference volume before damage and D_n is the damage variable in the direction of the normal vector n. Lemaitre's model assumes that the distribution of damage in the material is isotropic. Therefore,

Fig. 5. Geometry of the three point bending test specimen (no. 8).

the value of the damage in all directions is the same and it can be represented by the scalar factor D, instead of D_n. In most of the applications, this is an acceptable assumption. It is also supposed that the value of the strain for a damaged material is equal to the value of the strain in the undamaged material with the stress value, known as the effective stress, defined by the following equation:

$$\sigma_{eff} = \frac{\sigma}{1-D} \tag{6}$$

where σ_{eff} is the effective stress.

According to Lemaitre's model, the damage evolution equation can be solved by the relevant equations of elastoplasticity. Eq. (7) shows the elastoplasticity and damage evolution equations according to Lemaitre's model [38]

$$\dot{D} = \frac{\partial F_D(Y, \overline{\varepsilon}, \dot{D}, \ldots)}{\partial Y} \dot{\varepsilon}(1-D) \tag{7}$$

where $\dot{D}$ and $\dot{\varepsilon}$ respectively show the evolution of the damage parameter and the strain. F_D represents the damage dissipation energy. Y and ε are respectively the damage energy release rate and the equivalent strain.

It is therefore necessary to solve a set of equations, which include the damage evolution and the plasticity equations in order to apply the CDM models.

4. Material characterization

4.1. Numerical models

All the experimental tests have been reproduced using finite element models. FE models of the tests are needed for the calibration of the MMC criterion; however the three point bending test has not been used for calibration but only for validation purpose (with some exception discussed herein). For the CDM calibration, just one FE model is strictly needed for the calibration (in the present case, the round smooth test) and the simulation of the other tests represents a validation of the damage model. Simulations of the MMC damage model have been performed using Abaqus 6.12 commercial software because of the availability of a specific MMC subroutine designed for Abaqus. Regarding the CDM approach, the Ls-Dyna solver has been used to perform the simulations due to the presence of the CDM framework among the solver options. Three dimensional finite element models of all specimens have been built and 8 node brick elements with reduced integration have been used. The same kind of elements have been used for the material calibration and for virtual testing purposes with excellent results in Bao and Wierzbicki [6], Giglio et al. [9], Giglio et al. [10], Gilioli et al. [11], Li et al. [38], and concerning the simulation of a ballistic impact Gilioli et al. [54]. Moreover, in [54] also an in-depth study of the mesh size sensitivity of C3D8R elements, adopted for the material calibration (both plasticity and ductile damage criterion) of an aluminum alloy, has been performed. The results showed how the chosen element types can properly be used in the framework of material characterization.

4.2. MMC material calibration

Ductile phenomenological criteria describe fracture without providing a physical explanation. In general terms, they are based on the definition of a cumulative damage parameter D as described

in Eq. (8)

$$D = \int_0^{\overline{\varepsilon}_f} \frac{d\varepsilon_p}{\varepsilon_f(\eta, \overline{\theta}, \dot{\varepsilon}_p, T)} \tag{8}$$

The parameter D is defined as the accumulation of the plastic strain increments ε_p weighted by a function called fracture locus ε_f. The two most influencing parameters of the fracture locus are the stress triaxiality η and the Lode angle parameter θ. The Lode angle is related to the third deviatoric stress invariant and has been already described in Eq. (2) so only a brief description of triaxiality is provided here. The stress triaxiality is a non-dimensional quantity, which accounts for the pressure effect on fracture and is defined in Eq. (9):

$$\eta = \frac{\sigma_h}{\sigma_{vm}}. \tag{9}$$

Taking simultaneously the Lode angle and triaxiality into account leads to a definition of a fracture locus, which is no longer a simple curve (like the Johnson–Cook one) but rather a surface in a 3D space described by triaxiality and Lode angle parameters (MMC).

The working mechanism of the damage phenomenological criteria, implemented into a numerical FE software, is based on the evaluation of the onset of fracture (damage initiation). When the parameter D, Eq. (9), reaches the conventional value of the unity, the corresponding failed element completely loses its stiffness and is suddenly eliminated from the analysis.

A reverse method approach, in which experimental tests are reproduced by means of numerical models in order to track the development of the stress/strain state up to failure in the critical locations thus acquiring the history of triaxiality and Lode angle during test, has to be adopted to calibrate the MMC criterion. Such quantities cannot be easily evaluated experimentally and hence FE models are essential.

The calibration approach followed in this paper is similar to the one used by Bao and Wierzbicki [35,36]. Each numerically simulated test can be summarized as a point inside the fracture locus plane. Each point η_{av}, $\overline{\theta}_{av}$, ε_f is obtained calculating the average stress triaxiality, η_{av}, the average Lode angle para-meter, θ_{av}, and evaluating the equivalent plastic strain (PEEQ) at the onset of failure, ε_f. These values are evaluated for the elements with the highest strain at the load step when the experimental data show the onset of failure. The average stress triaxiality, η_{av} and the average Lode angle parameter, $\overline{\theta}_{av}$ have been calculated following Bao's approach [35] following Eqs. (10) and (11):

$$\eta_{av} = \frac{1}{\varepsilon_f} \int_0^{\varepsilon_f} \eta \, d\varepsilon_p \tag{10}$$

$$\overline{\theta}_{av} = \frac{1}{\varepsilon_f} \int_0^{\varepsilon_f} \theta \, d\varepsilon_p. \tag{11}$$

The free parameters C_1, C_2, C_3 (see Eq. (4)) have been determined by means of a Matlab subroutine following the approach of Luo [47]: the fracture surface has not been fitted by using only the average fracture values of triaxiality and Lode angle but by considering the complete load history. This approach is summarized in Eq. (12)

$$Min(error) = Min\left[\frac{1}{N}\left(1 - \sum_{i=1}^{N} \int_0^{\overline{\varepsilon}_f} \frac{d\varepsilon_p}{\varepsilon_p}\right)^2\right]. \tag{12}$$

A summary of the results of the entire test/simulation program is shown in Fig. 6. The figure reports the evolution of the plastic strain ε_p (equivalent plastic strain, PEEQ) versus triaxiality and versus Lode angle, obtained from each numerical simulation of the experimental tests. Furthermore, the average stress triaxiality, η_{av},
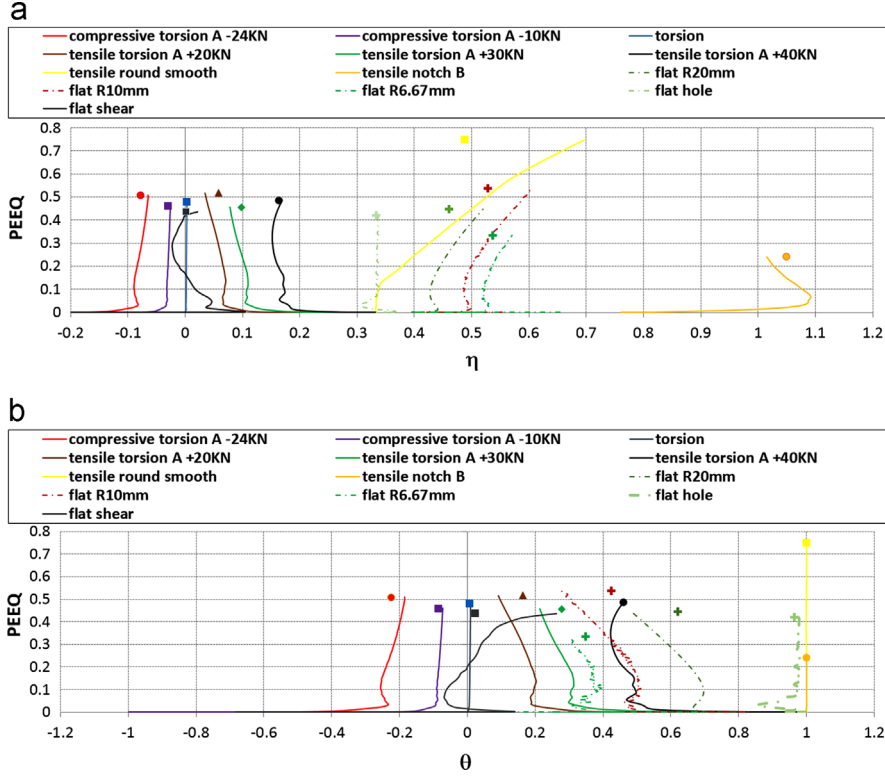
Fig. 6. Triaxiality versus PEEQ (a) and Lode angle versus PEEQ (b) evolution curves for all the tests.

and the average Lode angle, $\overline{\theta}_{av}$, and the equivalent plastic strain at the onset of the failure ε_f, are reported for each test.

According to Eq. (14) also two other parameters are fundamental in the MMC formulation: A, n.

In order to be consistent with the MMC formulation reported in Eq. (4) it is necessary to assume a power law to describe plasticity as expressed in Eq. (13):

$$\sigma = A(\varepsilon_e + \varepsilon_p)^n. \tag{13}$$

In [35,45,47–49,54] the authors showed that there is currently no optimized plasticity model which allows perfect fitting of the flow stress for all the different load cases. Indeed, for titanium not only fracture is affected by triaxiality and Lode angle but also the plasticity behavior. The assumption that the constitutive law obtained from the tensile test on the smooth specimen is able to reproduce the behavior of all the different tests can potentially lead to some errors in the evaluation of the load/displacement history during the calibration stage. On the other hand assuming different constitutive sets of parameters for each load configura-tions is not feasible for real industrial applications. In the present paper this issue has been resolved by determining an average constitutive law which is a compromise between all the optimized ones (one specific set of plasticity parameters for each test) and is thus able to reduce the overall error in all of the simulations.

In Table 3, the results of the calibration (base calibration, 13 experimental points) in terms of the constitutive law and the fracture parameters are presented.

In Fig. 7, the MMC fracture surface is shown. The filled black circles represent the average fracture point. It is important to underline that the lack of an exact overlap of the fracture surface with the average point is caused by the approach followed to obtain the fracture surface. The average points provide a quick overview of the Lode angle/triaxiality state at fracture but they do not form the base for the interpolation: the complete load history has been taken into account for the interpolation.

Table 3
MMC calibrated parameters.

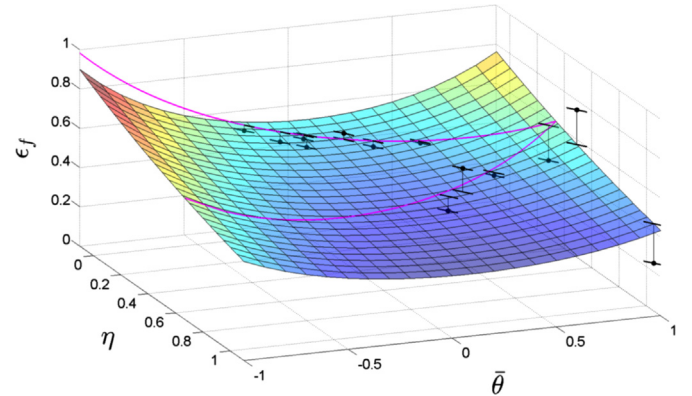| A [MPa]	n	ε_e	C_1 [dimensionless]	C_2 [MPa]	C_3 [dimensionless]
1470	0.1659	0.06376	0.04123	706.86	0.9339

Fig. 7. MMC fracture surface with a superimposed error bar between the average points and the fitted surface.

For a plane stress load condition a unique relation between the triaxiality and the Lode angle parameter, see Eq. (14), can be determined and thus the strain at failure can be described as a function of only the triaxiality. This relation is described by the light purple straight line in Fig. 7.

$$-\frac{27}{2}\eta\left(\eta^2 - \frac{1}{3}\right) = \cos(3\theta) = \sin\left(\frac{\pi\overline{\theta}}{2}\right) \tag{14}$$

4.3. Calibration of the CDM model

Exploiting *MAT_104 in LS-DYNA, Lemaitre's damage model has three parameters (ε_{th},S,D_{cr}) which have to be calibrated for each material:

- ε_{th} is the threshold strain. Damage starts when this value is reached.
- D_{cr} is the critical value of damage. Failure occurs when damage is equal to this value.
- S is a parameter related to the evolution of damage.

When adopting the MMC approach, in order to be consistent with the model assumptions, it is necessary to adopt a power law to describe plasticity. When adopting the CDM framework this limitation is no longer present. Indeed, the authors decided to adopt a hardening plastic constitutive law with the general form described by Eq. (15)

$$\sigma = \sigma_{y0} + Q_1(1 - \exp(-C_1\varepsilon_p)) + Q_2(1 - \exp(-C_2\varepsilon_p)). \tag{15}$$

It is worth remembering that the CDM is a coupled approach to damage hence there are interactions between the plasticity behavior and failure. In total, there are eight parameters to define: five are derived from plasticity and three come from failure. An inverse method has been used to calibrate Lemaitre's model. Smooth round specimens have been chosen as the reference calibration experiment. The specimen geometry is shown in Fig. 8.

The method applied in this paper, has been previously used also by other authors including Li et al. [38]. The fitting procedure has been performed by initially developing the FE model of the tensile test on the smooth specimen using the commercial non-linear software Ls-Dyna and then by means of its optimization environment Ls-Opt. Ls-Opt adopts an optimization scheme based on the minimization of the mean square error between FE and experimental load–displacement curves. It is important to remark that the calibration takes the simultaneous effect of the parameters on both plasticity and failure into account. Table 4 shows the obtained parameters for the model after the calibration. Fig. 9 shows a comparison between the experimental load–displacement data and the numerical results (if the round smooth specimen), which has been obtained from the calibrated models for the CDM and MMC. The adoption of the calibrated parameters leads to good agreement between the numerical and experimental load–displacement curves with regards to the plastic behavior and the displacement at failure in the CDM model. However, due to the fact that the MMC model has been calibrated using different experimental data, some differences between the experimental data and numerical results obtained from the MMC are considered reasonable.
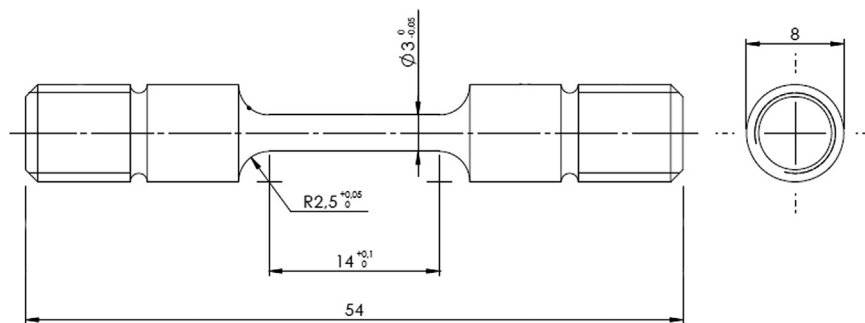
5. Results and discussion

5.1. Evaluation of the experiments based on the stress triaxiality and lode angle

Triaxiality versus PEEQ and Lode angle versus PEEQ has been shown in Fig. 6 in Section 4.2. These data have been obtained in the FE models analyzing the critical element with the highest PEEQ. An effective summary of the average values of triaxiality and Lode angle for each test is reported in Fig. 10. This figure is very important because it immediately shows the distribution of the tested configuration in terms of Lode angle and triaxiality. It is evident that every test, excluding the tensile ones on round specimen, correctly belongs to the plane stress curve (solid light blue line in Fig. 10, evaluated by Eq. (14)). This conclusion is obvious for flat specimen but it also applies to round specimen subjected to multi-axial loads. In these specimens, a crack starts from the outer surface due to the nature of the load, which consists of a superimposed axial constant load followed by an incremental torque, and hence it again represents a plane stress state (there is no external pressure applied).

The average triaxiality and the Lode angle for each test are distributed over a large area, as shown in Fig. 10, demonstrating that the experimental program covers a very wide field of stress

Table 4
Material model parameters for Lemaitre's model.

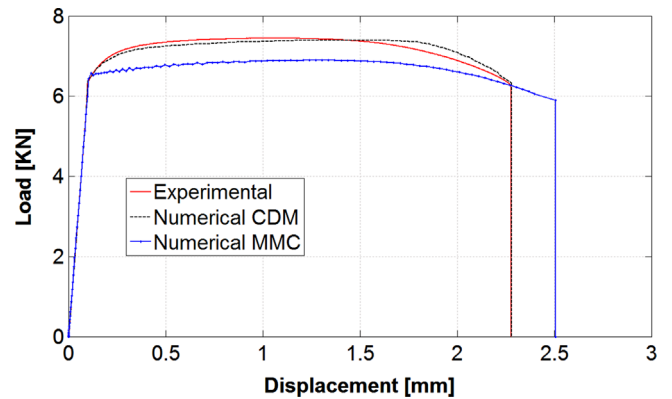| Plasticity					Damage		
σ_{y0} [MPa]	Q_1 [MPa]	C_1	Q_2 [MPa]	C_2	ε_{th}	S [MPa]	D_{cr}
912.712	499.715	3.627	103.215	146.212	0.2	25	0.1356

Fig. 9. Comparison between the experimental and numerical (CDM and MMC) load–displacement curves for the smooth specimen adopted for the CDM calibration.

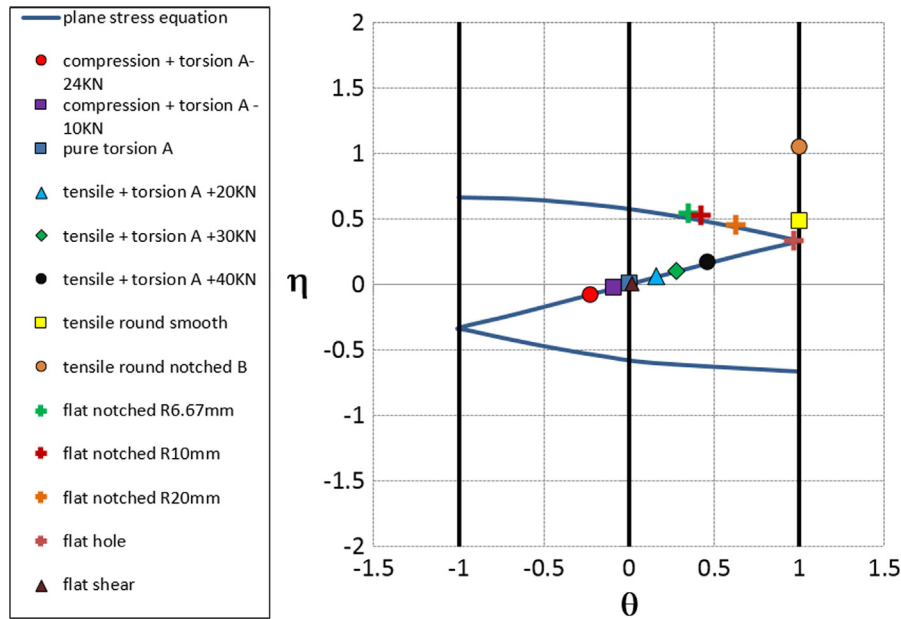**Fig. 8.** Geometry of the round smooth specimen.

Fig. 10. Average triaxiality–lode angle in the experiments. (For interpretation of the references to color in this figure, the reader is referred to the web version of this article.)

states. Further evidence of the accuracy of the modeling regards the pure torsion and the shear test of the flat specimen, whose values of triaxiality and Lode angle are almost zero as expected from the theory concerning the shear dominant failure.

Scanning electron microscope (SEM) images of the failure surface of the specimens (Fig. 11) have been acquired to evaluate the possible effect of the abovementioned different stress states on the specimen fracture surface. In the notched flat specimens, many dimples of varying size and secondary cracks are present on the failure surface of the specimens, see Fig. 11c–e. This surface morphology is typical of a mostly ductile fracture and hence it is possible to state that the flat notched specimens have a ductile fracture. However, in some cases the fracture surface exhibits also some partially brittle ruptures even if the fracture is mainly ductile. Among the notched flat specimens, the specimen with a 20 mm notch radius (no. 1, Table 2), which has the smallest triaxiality value, has a more ductile failure surface with less micro cracks present on the failure surface. The failure surface of the flat specimen with a hole (no.) is quite similar to the notched flat specimens, see Fig. 11(b). Also in this case micro cracks are detectable on the failure surface. However, it seems that the failure mechanism is more ductile compared with the notched flat specimens (the triaxiality is lower for the flat specimen with a hole, see Fig. 10). The failure surface of the shear specimen (no. 5) is different from the other flat specimens, see Fig. 11(a). The average triaxiality and Lode angle values are close to zero in the shear specimen and are therefore very distant from the other tested flat configurations. The shear morphology area is deformed by shear stresses and is stretched along the applied load, with no detectable cracks present on the failure surface.

In the torsion+tension tests (B+20 kN, B+30 kN and B+40 kN), see Fig. 11(g,h) the value of triaxiality is higher than for the pure torsion test and increases for the higher tensile load (triaxiality spacing between 0 and 0.2, Fig. 10) due to the existence of a constant tensile preload. In the multiaxial torsion tests, failure is characterized by several dimples on the failure surface. No micro-cracks exist on the surface and the dimples are relatively uniform in size without the presence of particularly large dimples. The overall size of the surface dimples is smaller in these test specimens compared with flat notched specimens. Sliding effects of the surfaces caused by shear are also evident on the failure surface of the multiaxial torsion tests

and it is evident comparing the different surfaces shown in Fig. 11 (g) and (h). The round notched specimen (no. 7) has a medium high triaxiality (around 1), see Fig. 11(f). The failure is ductile with a typical dimple rupture, which indicates that tensile stress is dominant. Many small dimples surrounded by larger ones are clearly visible.

5.2. Comparison of the experimental and numerical results

The capability of the damage models to correctly predict the displacement (rotation) at failure and the failure location in the specimens has been investigated comparing numerical results with experimental ones. Figs. 12 and 13 show the load–displacement (torque–rotation) data obtained from the experiments and the numerical simulations adopting both MMC and CDM damage models. It is worth to underline that such type of assessment is not a real validation (as it has not been performed with independent data from the calibration) but is a very effective indicator of the goodness of the models (formulations and parameters). The performance of the present models (calibrated with very few parameters), in replicating very different loading conditions (13 different loading conditions for triaxility and load angle) is a good indicator of their capabilities in replicaring the physical phenomena under investigation, see Figs. 9, 12 and 13 and Table 5.

According to the von Mises yield stress criterion (adopted for the all the reported analysis), the hydrostatic stress (first invariant of the stress tensor, J1) and the third invariant of the stress deviator (Lode parameter, J3) are assumed to have no effect on plasticity. However, research has shown that a variation of the stress triaxiality and the Lode angle can affect the plastic behavior of some materials [47–50]. In order to produce accurate load–displacement data for each test in the plastic region, it should be necessary to use a specifically calibrated plastic law for each test. The visible difference in Figs. 12 and 13 between the experimental and the numerical load–displacement results in the plastic region is hence due to the adoption of an individually calibrated plastic constitutive law which does not perfectly fit the material plastic behavior and is not related to the damage models themselves. Table 5 summarizes the average error in the plastic region between the experimental and numerical load–displacement/torque–rotation data. The error has been calculated as the perceptual average difference between the numerical and the experimental curve, up to the failure point.
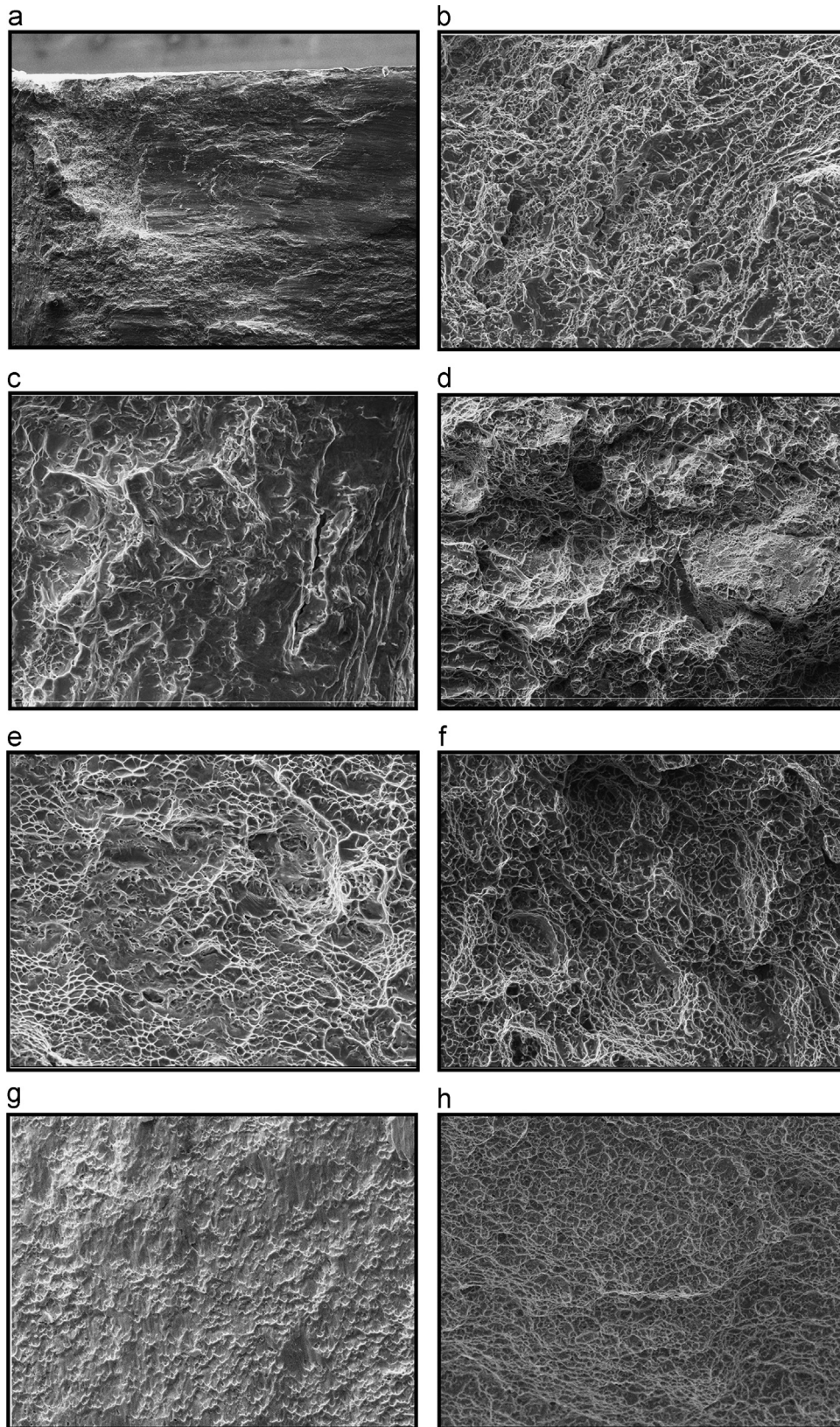
Fig. 11. SEM photos of the failure surface of specimens: (a) flat shear 150 ×, (b) flat hole 650 ×, (c) flat notched 10 mm 1200 ×, (d) flat notched 6.67 mm 600 ×, (e) flat notched 20 mm 1290 ×, (f) round notched 1000 ×, (g) border area and (h) center area of the torsion+30 kN 1000 ×.

Figs. 12 and 13 clearly show that neither the MMC nor the CDM model predictions for the failure displacement are perfectly in agreement with the experimental results. A change of the geometry affects the damage model parameter calibration. However, this

difference between the numerical and experimental failure displacement/rotation, which has been summarized also in Table 5, has two different causes in the MMC and CDM models. In the MMC model it is due to the fact that all experimental results have been
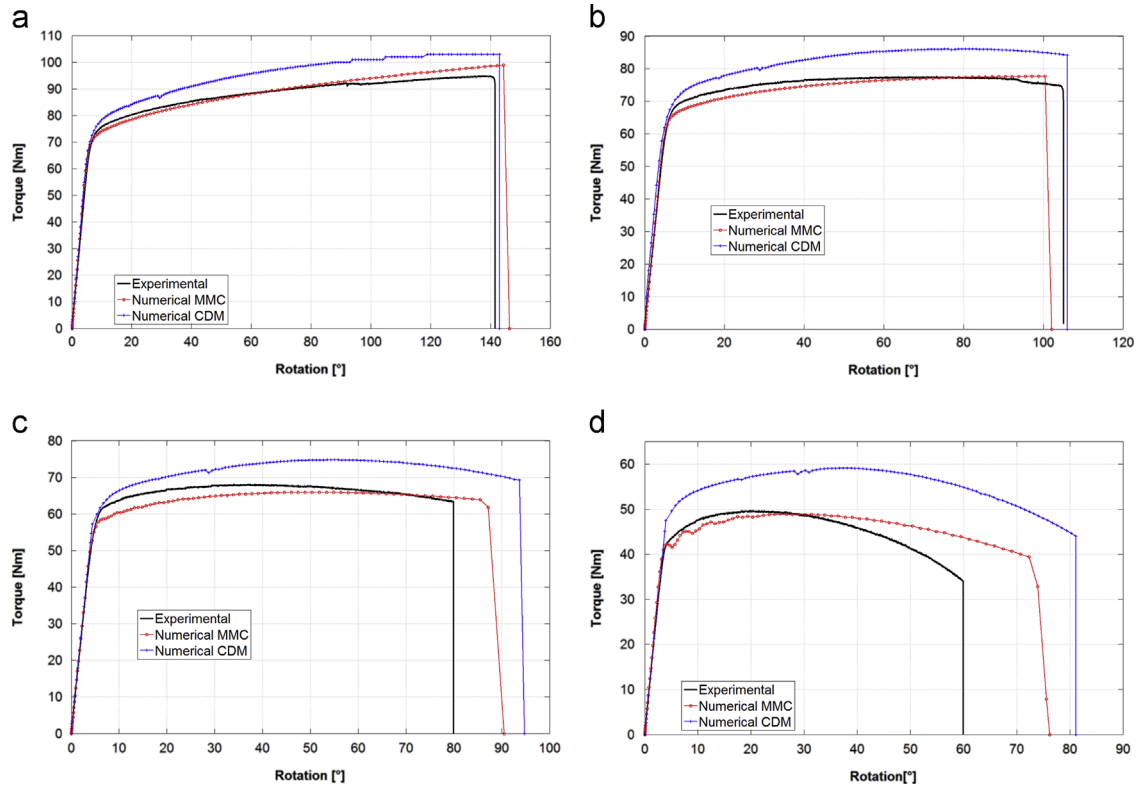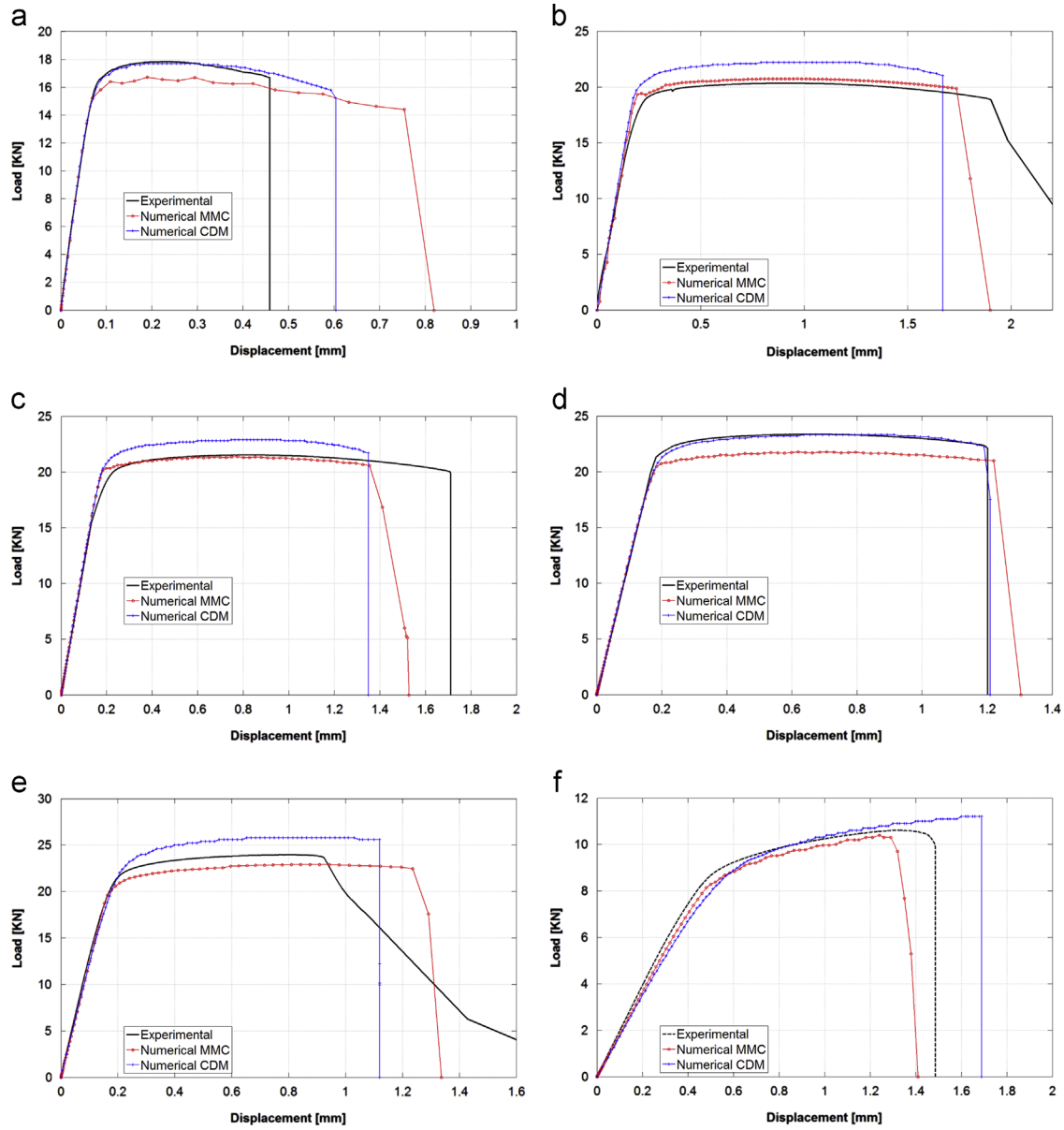
Fig. 12. Comparison of the experimental and numerical torque–rotation curves for the multiaxial torsion tests: (a) pure torsion, (b) torsion+20 kN tension, (c) torsion+30KN tension, and (d) torsion+40 kN tension.

used for the calibration (more detailed information about the calibration process can be found in Section 4.2), but the fracture surface is defined by minimizing the error among all the estimated failure points. The MMC fracture has a fixed equation for fracture based on just three constants. The model hence has a limited flexibility to fit data. The final fracture surface is thus a compromise leading to the minimum global error even if for some tests the error can potentially reach a relevant value. In the CDM model, only the smooth specimen has been used for the calibration (see Section 4.3) and the error between the predictions of the FE model and the experimental results is only due to the fact that one calibration in a specific loading condition does not exactly fit all the other loading conditions. It is interesting to highlight that in the presence of an important discrepancy between the results obtained by the MMC model, a similar relevant discrepancy is also evident in the CDM model results.

Fig. 14 shows the error on the estimation of the displacement/rotation at failure versus the triaxiality and Lode angle for the MMC and the CDM models according to Table 5. The red line in these figures indicates a 20% error limit. The error value for both the MMC and CDM models is in most cases less than 20%, see Fig. 14, and therefore guaranties a reasonable accuracy for the different loading conditions. In some cases, the models predict the failure displacement/rotation with very high accuracy (less than 5% error). However, in two regions of triaxiality (quite low and very high triaxiality) both models fail to provide appropriate predictions and the error is above 20%, and in some cases reaches 50%. In the literature, the loading condition is commonly described using triaxiality rather than the Lode angle and therefore, also in this paper, the results are discussed mostly on the basis of triaxiality. The error is high in the triaxiality region of 0.15–0.35. The CDM model predictions show the highest error of 35% for the multiaxial test with a superimposed tension of 40 kN (average triaxiality of 0.164). Also, the two experimental points which are

close to this critical point show a relatively high error (17.5 and 21.7%), as can be seen in Fig. 14(a). The transition of the failure mechanism from a shear dominant failure to a failure driven mainly by tension is potentially the cause of this error. As mentioned in Section 5, SEM photos also demonstrate that the failure surface for the multiaxial specimens is different compared with the surface of uniaxial test specimens. Lemaitre's model is based on the creation and evolution of dimples inside the material and dimple fracture is considered the main failure mechanism. Therefore, when the failure phenomenon is different, the model can produce errors.

At very high triaxiality (around 1), which is related to the tensile test of the round notch specimen B, both models show a relevant error (higher than 20%) in the prediction of the failure displacement/rotation. The MMC and CDM models respectively reproduce such a test with a 52.17% and 31.25% error. This error is potentially linked to the experimental test data used to calibrate the MMC and CDM models. As already reported, the fracture locus for the MMC model is a surface, which has been obtained by curve fitting of the experimental data. Therefore, experimental points, which have been chosen for the fitting procedure, play an important role in the final shape of the fracture locus and affect the predictions of the model. If the experimental data focus on some localized regions, the fracture surface obtained is very accurate for the loading conditions close to this region but in other areas, the error is potentially very high. As can be seen in Fig. 10, most of the experimental points which have been used in this research for the calibration of the MMC model are far from the very medium-high triaxiality region which is related to the tensile test of the round notched specimen B. Therefore, it is reasonable that the MMC model predicts this experiment with less accuracy compared with the other experiments. The reason for the high error of the CDM model it is also related to the calibration. As it has been explained in Section 4.2, a tensile test of the round

Fig. 13. Comparison of the experimental and numerical load–displacement graphs in the tension tests (a) round notched specimen B, (b) flat notched radius 20 mm, (c) flat notched radius 10 mm, (d) flat notched radius 6.67 mm, (e) flat with hole, and (f) flat shear.

Table 5
Average errors of numerical simulations compared with experimental data.

Specimen number	Average triaxiality	Average lode angle	Failure displacement		Plasticity	
			MMC error [%]	CDM error [%]	MMC error [%]	CDM error [%]
Flat specimen no. 1	0.459	0.62	6.31	8.42	2.1246	9.1665
Flat specimen no. 2	0.528	0.425	17.54	21.05	0.9746	6.0407
Flat specimen no. 3	0.537	0.348	1.67	0.83	6.5676	0.3191
Flat specimen no. 4	0.334	0.964	34.784	21.74	4.5772	7.1518
Flat specimen no. 5	0.0015	0.022	30.774	14.61	2.9941	2.0467
Pure Torsion (no. 6)	0.00219	0.0067	2.13	1.42	1.7668	7.9924
Torsion+20 kN tension (no. 6)	0.0577	0.163	3.33	0.95	1.7713	9.3204
Torsion+30 kN tension (no. 6)	0.0983	0.278	8.75	17.5	2.8987	9.1287
Torsion+40 kN tension (no. 6)	0.164	0.4608	20	35	6.1768	26.1328
Tension test (no.)	1.049	0.9998	52.17	31.52	5.8622	0.9387

smooth specimen has been used for the calibration of the CDM specimen. Again in this case, the high triaxiality value in the notched round specimen B is far from the calibration point potentially causing this error in the model's prediction.

The discussion about the error trend for both models highlights that when moving to practical applications of the damage models, also the design of the experimental program plays a critical role. Hence, it is important to remark that damage models should be
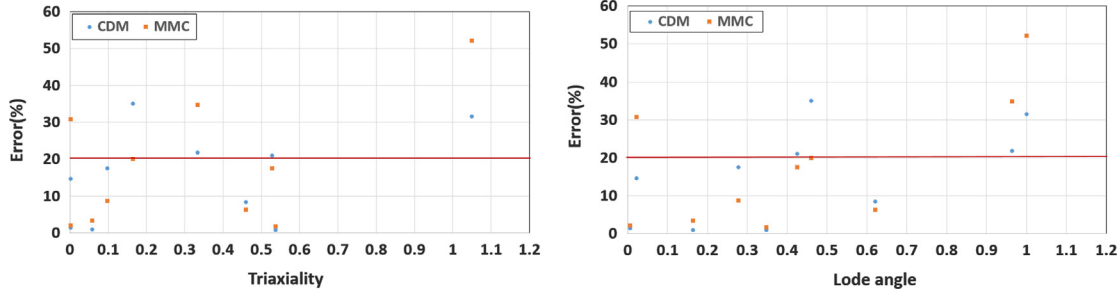
Fig. 14. (a) Error on the displacement/rotation at failure versus triaxiality and (b) error on the displacement/rotation at failure versus Lode angle for both the MMC and the CDM models.

used very attentively when applied to describe scenarios far from the calibration conditions.

5.3. Evaluation of the damage initiation location

The prediction capacity of both the MMC and the CDM models with regards to the damage initiation point has also been evaluated. In the torsion tests, both models estimate a point on the outer surface in the middle cross section of the specimen as the failure initiation location. Similarly to the experimental results, a crack is predicted to start from this area and to then propagate towards the center of the specimen. In the tensile tests using flat specimens (except the shear specimen) both models predict that failure occurs in the middle cross section, which has the minimum surface area. The initial point of the damage is the center/core of the section and damage evolves from the core outwards. This behavior has been confirmed experimentally in the present work and in the work by Dunand and Mohr [51]. They performed some experimental tests on similar flat specimens made from TRIP780 steel and verified that cracks started from the center of the specimen. The shear specimen shows a different fracture initiation location compared with the other flat specimen. For this specimen both models predict that the critical point is located at the edge of the specimen in the shear region and not in the center. Also Li et al. [38] reported the same phenomenon on similar specimens made from Al6061. Fig. 15 shows the shear specimen and critical region before and after failure obtained adopting the CDM model.

6. A more complex application: three point bending test

So far, the material calibration has been discussed but finally in the following sections its accuracy in an application characterized by a high stress/strain gradient is assessed: a three point bending test on a sharp notched specimen (see Section 2.3). The FE model has been based on solid 3D elements with a reduced integration scheme and quasi static explicit analyses have been carried out to reproduce the non-linear phenomena taking place during the test. Numerical and experimental load–displacement curve have been compared and different mesh sizes have been tested. Table 6 shows the error of the predictions of both models for the failure displacement in the three point bending test obtained from the finite element models with different mesh sizes.

The results of both models highlight two particular aspects concerning the overall accuracy and a strong mesh size effect in the simulations. Mesh dependence is a well-known effect of the application of ductile damage criterion in the presence of a sharp notch. It results in the estimation of the displacement at failure without a convergence value: decreasing the mesh size always leads to an earlier displacement at failure. This topic has been highlighted in [11] for the simulation of a fracture toughness test on an Al6061-T6 CT specimen, and Kim et al. [52] and Kim et al.

[53]. It is evident that neither the calibrated MMC and nor the CDM model can satisfactorily reproduce the TPBT fracture. It is necessary to more carefully analyze the stress state of the TPBT in order have a clearer image of the possible sources of these discrepancies.

The stress state for the TPBT varies greatly depending if it is considered for a region very close to the notch or for a region a little bit further inside the specimen (0.3 mm), Fig. 16. It is evident that near the notch, the stress state is more similar to the flat specimen with a 6.6 mm radius notch but moving away from the notch the stress state tends to become more similar to the round tensile test on the notched specimen (geometry B). In any case, the predicted TPBT lies within a region quite far from the experi-mental point. The fracture surface in this area, according to the MMC theory, is simply an extrapolation based on the calibration equation. As already mentioned in Section 5.2, the calibration procedure for the MMC model evidently leads to a fracture locus which guarantees good results especially in the area where a lot of experimental data is located. So knowing that the TPBT stress state is closer to flat and round tensile tests rather than to multiaxial tests, therefore, the pure torsion, the multiaxial and the shear test have been neglected and a new calibration has been performed, Fig. 16. Data of the new calibration are reported in Table 7 labeled as optimal calibration. Table 7 also contains a second calibration based on all the experimental data including the TPBT. The idea is to check the sensibility of the calibration adding one single point. Very small differences between the original calibration and the one including TPBT are visible. These differences are related to the number of points evaluated for the calibration: the base calibra-tion is obtained using 13 tests thus adding one single point (TPBT) does not significantly affect the calibrated fracture surface (see coefficients of the second and fourth column of Table 7).

The subsequent simulation of the TPBT has been carried out adopting the optimal calibration for TPBT and the results are shown in Fig. 17. Again, the mesh size effect is evident (it is not avoidable) but the results are in much better accordance with the experimental data. The error on the estimation of the displace-ment at failure using the new calibration is reported in Table 9.

Also the CDM calibration can be improved to have a material model which describes the TPBT load scenario more accurately. Following a trial and error approach, a new series of damage model parameters has been chosen for the CDM model. Table 8 shows the new CDM damage model parameter values. Changing the threshold strain (ε_{th}) strongly affects the behavior of Lemaitre's damage model. Physically, ε_{th} indicates the value of the strain at which damage starts. Generally, the value of the failure strain decreases with the increment of the triaxiality. According to this fact, the value of the threshold strain has been reduced in the new model parameters, to 0.1. The value of the parameter S has also been reduced according to the reduction of ε_{th}. The aim of this new calibration is to show that, with the appropriate parameters, also Lemaitre's model is able to accurately predict the failure point
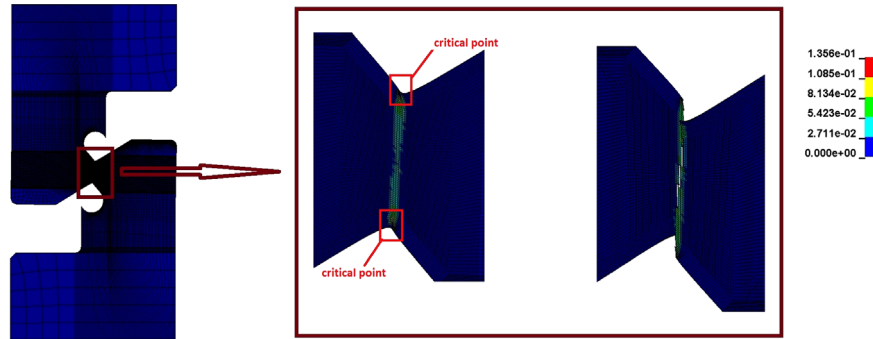
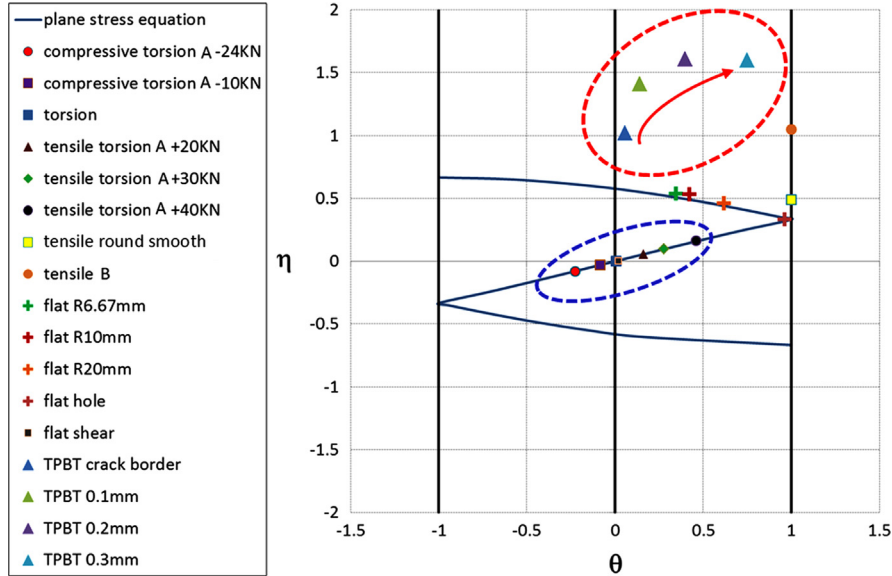**Fig. 15.** Damage contour in the shear specimen (CDM).

Fig. 16. Summary of all the experimental tests including the TPBT (triangular marks). In the red ellipse the TPBT values have been evaluated at various distances away from the notch. In the blue ellipse, the experimental points have been neglected for the new calibration. (For interpretation of the references to color in this figure legend, the reader is referred to the web version of this article.)

Table 6
Error of numerical prediction compared with experimental results for the simulation of the three point bending test (original calibration) using the CDM and the MMC framework.

	MMC			CDM		
Mesh size [mm]	0.05	0.1	0.5	0.075	0.1	0.2
Error [%]	50	90	200	90	110	290

Table7
New MMC calibration data.

Parameters	Base calibration	Optimal calibration for the TPBT	Base calibration including the TPBT
A [MPa]	1470	1470	1470
n	0.1659	0.1659	0.1659
ε_e	0.06376	0.06376	0.06376
C_1	0.04123	0.17562	0.05343
C_2	706.86	865.96	719.71
C_3	0.9339	0.99892	0.9493

in the three point bending test. This discussion is however emphasizes that the geometrical transferability of the CDM parameters
is not guaranteed for Ti–6Al–4V: the direct application of the calibration obtained using just the smooth specimen leads to
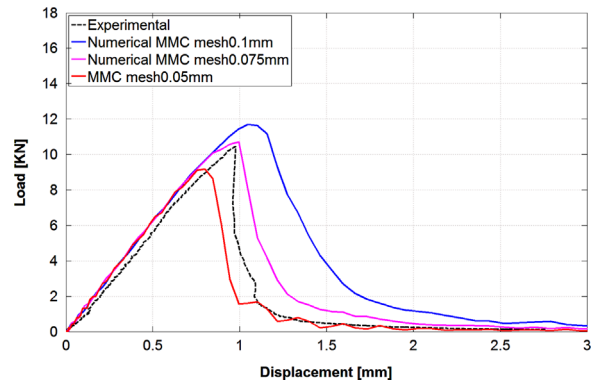

Fig. 17. Comparison between the numerical and the experimental load–displacement curves for the TPBT, adopting the newly calibrated MMC criterion.

Table 8
New calibration of CDM model parameters.

ε_{th}	S [MPa]	D_{cr}
0.1	7.5	0.1356

inaccurate results if applied to the TPBT. The experimental and numerical load–displacement curves obtained with the new damage model parameters are shown in Fig. 18 while the error
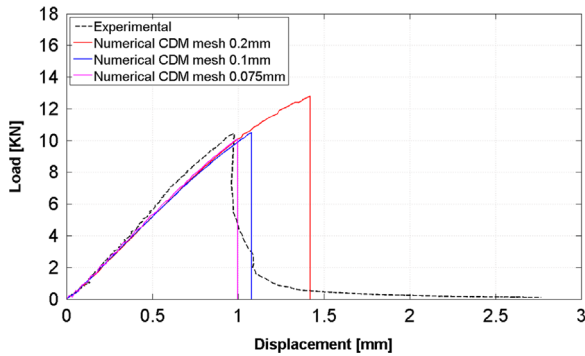
Fig. 18. Comparison of the numerical and the experimental load–displacement curves for the TPBT adopting the newly calibrated CDM criterion.

Table 9
Failure displacement errors of numerical analysis using the CDM and MMC framework compared with the experimental three point bending test. The optimal calibration for the TPBT has been used for both models.

	MMC			CDM		
Mesh size [mm]	0.05	0.075	0.1	0.075	0.1	0.2
Error [%]	−11.22	3.675	13.15	0.478	3.349	22.48

on the estimation of the displacement at failure using the new calibration is reported in Table 9.

With the new calibration of both the MMC and CDM models, the numerical results fit the experimental load–displacement curve well. In accordance with the previous discussion, it is important to clearly comment on the possible consequences of adopting an MMC or a CDM ductile criterion. First of all, scholars should be aware of the mesh dependence in case of a sharp notch. Instead, if there is a round notch the mesh effect is negligible. The second aspect to take into account regards the dependence of the fracture surface on the available experimental points for the calibration of the MMC model. Indeed, from an experimental point of view it is difficult to have data spaced on a homogeneous grid. It is clear that the calibration is much more accurate in a region where a higher number of test results are located. For the CDM model it is important to remark that only one test is necessary to completely assess the material parameters but its correct choice is fundamental. A calibration test, which is relatively close to the real application stress state, is much more trustworthy as it reduces errors linked to the geometrical transferability.

7. Conclusion

The modified Mohr Coulomb and Lemaitre's damage models have been calibrated for the widely used Ti–6Al–4V titanium alloy. A large experimental program has been carried out and the calibrated material models have been implemented into finite element analyses. Comparisons of the numerical and experimental results demonstrate that both the MMC and the CDM models are able to predict the failure displacement in most of the experiments with an error of less than 20%. In general, whenever the MMC prediction results in large errors, the CDM also fails to provide appropriate predictions for the failure displacement. For the stress triaxiality values around 0.2 and larger than 1, both models overestimate the failure displacement by an error of more than 20%. This demonstrates that for practical applications, special attention has to be paid when the loading condition is close to either the high or the low triaxiality region.

It is very difficult to define a unique set of MMC and CDM parameters unless some discrepancies are accepted. The availability of a large number of data determines the accuracy of the MMC, allowing the definition of a more precise fracture locus. This approach cannot always be followed in an industrial scenario where in order to reduce costs and time, only the minimum number of tests has to be performed. Therefore, a preliminary evaluation of the stress state of the application object of the study is recommended. The following calibration should be based on tests having a triaxiality/Lode angle not too different compared with the application. Concerning the CDM model, it can be calibrated using one straightforward experiment, however it is worth mentioning that when the loading condition is far from the calibration, additional errors can occur in the prediction of Lemaitre's model because the geometrical transferability is not always fully guaranteed. From a practical point of view, it is better to choose the calibration test close to the real application loading condition to guarantee appropriate accuracy of the results.

Concluding, the present research wants to show the advantages of the adoption of the MMC and the CDM approaches in numerically reproducing ductile fracture. Among the positive points, it is worth mentioning that the evaluated models are based on very few parameters, a limited number of experimental tests and their algorithms are already implemented in many FE commercial software. On the other hand, such models have also various critical weak aspects. For instance in case of the simulation of sharp-notched specimen, a strong mesh size effect without a clear convergence threshold level exists. Moreover, the accuracy of the simulations for a general application strongly depends on the initial calibration program because the geometrical transferability is not straightforward. However, drawing a final balance between advantages and disadvantages, the authors believe that the CDM and the MMC are the most promising and effective ductile damage criteria currently available.

Acknowledgment

References

[1] Johnson GR, Cook WH. Fracture characteristics of three metals subjected to various strains, strain rates, temperatures and pressures. Eng Fract Mech 1985;21:31.
[2] Rice JR, Tracey DM. On the ductile enlargement of voids in triaxial stress fields. J Mech Phys Solids 1969;17:201.
[3] Leroy G, Embury JD, Edward G, Ashby MF. A model of ductile fracture based on the nucleation and growth of voids. Acta Metall 1981;29:1509.
[4] Cockcroft MG, Latham DJ. Ductility and the workability of metals. J Inst Met 1968;96:33.
[5] Bao Y, Wierzbicki T. A comparative study on various ductile crack formation criteria. Trans ASME 2004;126:314.
[6] Bao Y, Wierzbicki T. On the fracture locus in the equivalent strain and stress triaxiality space. Int J Mech Sci 2004;46:81.
[7] Bai Y, Wierzbicki T. A new model of metal plasticity and fracture with pressure and lode dependence. Int J Plast 2008;24:1071.
[8] Bai Y, Wierzbicki T. Application of extended Mohr–Coulomb criterion to ductile fracture. Int J Fract 2010;161:1.
[9] Giglio M, Manes A, Vigano F. Ductile fracture locus of Ti–6Al–4V titanium alloy. Int J Mech Sci 2012;5:121.
[10] Giglio M, Manes A, Vigano F. Numerical simulation of the slant fracture of a helicopter's rotor hub with ductile damage failure criteria. Fatigue Fract Eng Mater Struct 2012;35:317.
[11] Gilioli A, Manes A, Giglio M. Numerical simulation of a fracture toughness test of an Al6061-T6 aluminium alloy using a ductile criterion. Mech Res Commun 2014;58:2–9.

[12] Gao X, Zhang G, Roe CH. A study on the effect of the stress state on ductile fracture. Int J Damage Mech 2010;19:75.

[13] Brunig M, Chyra O, Albrecht D, Driemeier L, Alves M. A ductile damage criterion at various stress triaxialities. Int J Plast 2008;24:1731.

[14] Zadpoor A, Sinke J, Benedictus R. Formability prediction of high strength aluminum sheets. Int J Plast 2009;25:2269.

[15] Gurson AL. Continuum theory of ductile rupture by void nucleation and growth, I. Yield criteria and flow rules for porous ductile media. J Eng Mater Technol 1977;99:2.

[16] Tvergaard V. Material failure by void growth of coalescence. Adv Appl Mech 1990;27:83.

[17] Lemaitre J. A continuous damage mechanics model for ductile fracture. J Eng Mater Technol 1989;107:83.

[18] Chaboche JL. Continuous damage mechanics—a tool to describe phenomena before crack initiation. Nucl Eng Design 1981;64:233.

[19] Kachanov, LM. Time of the rupture process under creep condition. TVZ Akad, s.S:r., OTD Ted Nauk, 8; 1958.

[20] Chandrakanth S, Pandey PC. An isotropic damage model for ductile material. Eng Fract Mech 1995;50:457.

[21] Bonora N. A nonlinear CDM model for ductile failure. Eng Fract Mech 1997;58:11.

[22] Tai W, Yang BX. A new damage mechanics criterion for ductile fracture. Eng Fract Mech 1987;27:371.

[23] Tai HW. Plastic damage and ductile fracture in mild steels. Eng Fract Mech 1990;36:853.

[24] Chow CL, Wang J. Anisotropic theory of continuum damage mechanics for ductile fracture. Eng Fract Mech 1987;27:547.

[25] Voyiadjis GZ, Park T. Kinematics of damage for finite strain elasto-plastic solids. Int J Eng Sci 1999;37:803.

[26] Lemaitre J, Desmorat R, Sauzay M. Anisotropic damage law of evolution. Eur J Mech A Solids 2000;19:187.

[27] Yang X, Li N, Jin Z, Wang T. A continuous low cycle fatigue damage model and its application in engineering materials. Int J Fatigue 1992;19:687.

[28] Pires FMA, de Sa JMAC, Sousa LC, Jorge RMN. Numerical modeling of ductile plastic damage in bulk metal forming. Int J Mech Sci 2003;45:273.

[29] Pirondi A, Bonora N. Modeling ductile damage under fully reverse cycling. Comput Mater Sci 2003;26:129.

[30] Bhattacharya B, Ellingwood B. A new CDM-based approach to structural deterioration. Int J Solids Struct 1999;36:1757.

[31] Jing J, Meng G, Sun Y, Xia S. An effective damage mechanics model for creep-fatigue life assessment of a steam turbine rotor. Int J Press Vessel Pip 2003;80:389.

[32] Hayhurst DR, Vakili-Tahami F, Zhou JQ. Constitutive equations for time independent plasticity and creep of 316 stainless steel at 550 °C. Int J Press Vessel Pip 2003;80:97.

[33] Choung CL. Comparative studies of fracture models for marine structural steels. Ocean Eng 2009;36:1164.

[34] Coppola T, Cortese L, Folgarait P. The effect of stress invariants on ductile fracture limit in steels. Eng Fract Mech 2009;76:1288.

[35] Wierzbicki T, Bao Y, Lee WY, Bai Y. Calibration and evaluation of seven fracture models. Int J Mech Sci 2005;47:719.

[36] Bao Y, Wierzbicki T. On the cut-off value of negative stress triaxiality for fracture. Eng Fract Mech 2005;72:1049.

[37] Bonora N, Ruggiero A, Esposito L, Gentile D. CDM modeling of ductile failure in ferritic steels: assessment of the geometry transferability of model parameters. Int J Plast 2006;22:2015.

[38] Li H, Fu MW, Lu J, Yang H. Ductile fracture: experiments and computations. Int J Plast 2011;27:147.

[39] Katani S, Madadi F, Atapour M, Ziaei Rad S. Micromechanical modelling of damage behavior of Ti–6Al–4V. Mater Design 2013;49:1016.

[40] ASME Metals Handbook Volume 2 – Properties and Selection: Nonferrous Alloys and Special-Purpose Materials.

[41] Mapelli C, Manes A, Giglio M, Mombelli D, Giudici L, Baldizzone C, et al. Survey about effects of shot peening conditions on fatigue performances of Ti–6Al–4V titanium alloy mechanical specimens featured by different cross-section geometries. Mater Sci Technol 2012;28:543.

[42] Giglio M, Gilioli A, Manes A. Mechanical behaviour of Al 6061-T6 aluminium alloy Under large strain and failure, Numerical Modeling of Materials Under Extreme Conditions. Advanced Structured Materials 2014;35:143, http://dx.doi.org/10.1007/978-3-642-54258-9_7.

[43] Barsoum I, Faleskog J. Rupture mechanisms in combined tension and shear experiments. Int J Solids Struct 2007;44:1768.

[44] Korkolis YP, Kyriakides S. Inflation and burst of anisotropic aluminum tubes for hydroforming applications. Int J Plast 2008;24:509.

[45] Zhao J. Applicability of Mohr–Coulomb and Hoek–Brown strength criteria to the dynamic strength of brittle rock. Int J Rock Mech Min 2000;37:1115.

[46] Palchik V. Application of Mohr–Coulomb failure theory to very porous sandy shales. Int J Rock Mech Min 2006;43:1153.

[47] Luo M. Anisotropic ductile fracture of metal sheets: experimental investigation and constitutive modeling. (Ph.D. thesis). MIT; 2012.

[48] Bai Y, Teng X, Wierzbicki T. Study on the effect of the third stress invariant on ductile fracture, report 151. Technical report. Cambridge, MA: Impact and Crashworthiness Laboratory, Massachusetts Institute of Technology; 2006.

[49] Yang F, Sun Q, Hu W. Yield criterions of metal plasticity in different stress states. Acta Metall Sin 2009;22:123.

[50] Gilioli A, Manes A, Giglio M, Allahverdizadeh N. Effect of triaxiality and Lode angle on the plasticity behavior of a Ti–6Al–4V titanium alloy. Key Eng Mater 2014;577–578:413.

[51] Dunand M, Mohr D. Hybrid experimental-numerical analysis of basic ductile fracture experiments for sheet metals. Int J Solids Struct 2010;47:1130.

[52] Kim JH, Kim NH, Kim YJ, Hasegawa K, Miyazaki K. Ductile fracture simulation of 304 stainless steel pipes with two circumferential surface cracks. Fatigue Fract Eng Mater Struct 2013;36:1067.

[53] Kim NH, Oh CS, Kim YJ, Yoon KB, Ma YH. Comparison of fracture strain based ductile failure simulation with experimental results. Int J Press Vessel Pip 2011;88:434.

[54] Gilioli A, Manes A, Giglio M, Wierzbicki T. Predicting ballistic impact failure of aluminium 6061-T6 with the rate-independent Bao–Wierzbicki fracture model. Int J Impact Eng 2015;76:207.